Photoionization and subsequent Auger decay of a K 2*s* vacancy

J. Soronen,[1] S.-M. Aho,[1] K. Jänkälä,[1] M. Huttula,[1] J-M. Bizau,[2,3] D. Cubaynes,[2,3] L. Andric,[4] J. Feng,[4] I. Ismail,[4] P. Lablanquie,[4] F. Penent,[4] and J. Palaudoux[4]

[1]*Nano and Molecular Systems Research Unit, University of Oulu, P.O. Box 3000, 90014 Oulu, Finland*
[2]*ISMO, CNRS UMR 8214, Université Paris-Sud, Bâtiment 350, F-91405 Orsay Cedex, France*
[3]*Synchrotron SOLEIL, l'Orme des Merisiers, Saint-Aubin, Boîte Postale 48, 91192 Gif-sur-Yvette Cedex, France*
[4]*Sorbonne Université, CNRS, Laboratoire de Chimie Physique–Matière et Rayonnement, 75005 Paris, France*

(Received 9 November 2023; accepted 22 December 2023; published 22 January 2024; corrected 7 February 2024)

The photoionization and subsequent Auger decay of the 2*s* subshell in vapor phase potassium are investigated using multielectron coincidence spectroscopy with synchrotron radiation. This method, capable of detecting multiple particles simultaneously, enables a comprehensive description of all cascade decay paths of the K 2*s* vacancy. It establishes, at each step of the 2*s* cascade decay, whether the outer 4*s* electron is a spectator or participates in the decay. The study determines the populations of the cascade final state and the different ionization rates. Experimental findings are compared with theoretical predictions derived from the multiconfiguration Dirac-Fock approach and previous observations of cascade processes in argon, emphasizing differences attributed to the presence of an additional 4*s* electron. The research contributes to our understanding of the electronic structure of potassium and quantum mechanical transition processes.

DOI: 10.1103/PhysRevA.109.013108

I. INTRODUCTION

Electron spectroscopy is a well-established method for studies of electronic structure. Since its inception in the 1960s by Turner [1] and Siegbahn [2], there has been continuous development of experimental techniques as well as theoretical methods. Modern radiation sources, such as the next generation multibend achromat magnetic lattice storage ring synchrotrons (e.g., MAX IV in Sweden [3]) and free electron lasers (see, for example, Ref. [4]), along with novel coincidence analyzers [5], enable the research of various, direct and indirect, multielectron processes arising from single or multiphoton excitations and ionizations.

Over recent decades, magnetic bottle based multielectron coincidence spectroscopy has been applied to a plethora of studies. These range, for example, from spectroscopy of the ionic state in multiply charged atoms [6–8] to direct double ionization studies [9–11], hollow molecules [12,13], the search for Cooper pair formation [14], and attosecond electron spin dynamics [15].

Potassium belongs to the alkali metal group, which means that its electronic configuration is like rare gas argon, except for one additional outer shell electron, i.e., [Ar] 4*s*. Studying the effect of a single electron above the closed shell structure provides fundamental knowledge of valence electron correlation. In argon, the 2*s* photoelectron spectrum consists of a single relatively wide peak corresponding to a short-living $2s^1(^2S)$ photoionization final state ($\Gamma = 2.25 \pm 0.5$ eV) [16]). In potassium, the 2*s* photoelectron line is divided into two components, (^1S) and (^3S), reflecting the coupling between the remaining 2*s* core electron and the outer valence 4*s* electron.

In Ar, the vacancy in the 2*s* subshell can decay by emitting an Auger electron through the highly efficient $L_1L_{2,3}M$ Coster-Kronig Auger decay process, in which a 2*p* electron fills the same shell hole while a valence shell electron is ejected [17–21]. A similar situation can be expected in potassium. However, the role of the outer 4*s* valence electron remains a question: Does it remain a spectator during Auger relaxation, or is it involved in the decay?

Previously, Palaudoux *et al.* [22] studied photoionization from the K 3*s* subshell and investigated the spectroscopic properties of the $3s^1$ (^1S) and (^3S) states. In their spectrum, the (^1S) and (^3S) components were well separated in energy ($\Delta E = 350$ meV), and the lifetimes of the states were found to be remarkably different due to the electron correlation effects. The subsequent Auger decay of the K^+3s^1 states has also been studied. Indirect experimental information exists on the K^+3s^1 states from ion yield measurements [23,24], and the Auger decay of the $K^+3s^1(^1S)$ state was observed in K^+/He collisions [25]. K^+3s^1 cross sections were calculated by Kupliauskiene [26].

In the present study, we investigate the photoionization of the 2*s* subshell in initially neutral atomic potassium and the subsequent Auger decay cascade paths of the $2s^1$ states using synchrotron radiation and a magnetic bottle spectrometer. The aim is to describe exhaustively all K 2*s* decay paths and the populations of cascade final states with different ionization rates. The experimental findings are compared with theoretical predictions obtained from the multiconfiguration Dirac-Fock (MCDF) approach, as well as previous observations of corresponding cascade processes in argon, emphasizing differences attributed to the presence of an additional 4*s* electron.

II. EXPERIMENTS

The experiments were carried out at the French national SR laboratory SOLEIL (Saint-Aubin, France) using the ultrahigh

resolution soft x-ray PLEIADES beamline (9−1000 eV). At this beamline, soft x rays with any polarization can be generated using an Apple II type permanent magnet HU80 (80 mm period) undulator, starting from 60 eV [27]. The storage ring operated in single bunch mode, providing a light bunch in every 1184 ns.

A magnetic bottle time-of-flight spectrometer called HERMES (high energy resolution multielectron spectrometer) [12,28,29] was utilized to detect all electrons emitted in coincidence following the absorption of a single photon. In this spectrometer, electrons are repelled from the ionization area by an inhomogeneous field of a strong permanent magnet (0.7 T) (magnetic mirror configuration). They are then guided through a 2-m-long solenoid (1 mT) towards the detector, which consists of microchannel plates (MCPs). A phosphor screen is used to visualize the electron impact image, aiding in optimizing the position of the permanent magnet in the ionization region. The time of flight for each electron is recorded by a time-to-digital converter with discretization step of 120 ps. Calibration and conversion to kinetic energy were achieved by measuring He 1*s* photoelectron spectra at different photon energies.

The relative energy resolution of the spectrometer is estimated to be $\Delta E/E = 1.6\%$ for electron kinetic energies $E > 1$ eV. The overall detection efficiency is deduced by comparing, at different excess energies, the number of Auger electrons of the argon $2p$ hole detected with and without coincidence with the $2p$ photoelectron. The obtained value is 65% ± 5%, remaining constant for electrons with less than 100 eV kinetic energy and slightly decreasing for higher kinetic energies. This allows effective detection of up to five electrons in coincidence. The experimental data were obtained without using a mechanical chopper [30], as the detection of a fast 2*s* photoelectron with a defined time of flight enables the reconstruction of the time sequence of all electrons produced in a 2*s* photoionization event.

To handle potassium, which is an alkali metal that reacts violently with moisture, an inert atmosphere (N_2 gas) was employed. Potassium vapor was generated using a resistively heated oven designed and constructed at LCPMR. The vapor was then effused through a heated tube, 1 mm in diameter and 15 mm in length, to maintain collimation of the vapor beam. The oven was covered with a water-cooled jacket to prevent heating of the permanent magnet [22].

III. CALCULATIONS

The eigenenergies of the ground and different ionized states of K were calculated using the well-known multiconfiguration Dirac-Fock (MCDF) method. The MCDF method is described in detail elsewhere (see, e.g., [31], and references therein), but the main principles are also summarized here. The radial wave functions of the one-electron spin orbitals were obtained using the GRASP92 program. The optimization of the radial wave functions was performed using the average level (AL) scheme, in which the average energy of the atomic state functions (ASFs) is minimized. The ASFs for bound states were obtained by diagonalizing the Hamiltonian matrix in the basis of *JJ*-coupled antisymmetric configuration state functions (CSFs) with the RCI program [31].

The Auger decay process is dealt with by the two-step model, where the number of emitted Auger electrons is proportional to the product of the initial 2*s* core ionization cross section and the relative Auger component rate. The Auger decay intensity is given by

$$n_{f\beta} = \frac{2\pi \sum_{l_A, j_A} \left| \sum_{\mu\nu} c_{f\nu} c_{\beta\nu} M^{\mu\nu}_{f\beta}(J_f, J_\beta) \right|^2}{P_\beta(J_\beta)} Q_\beta(J_\beta), \quad (1)$$

where $P_\beta(J_\beta)$ is the total decay rate and $Q_\beta(J_\beta)$ is the $|\Psi(J_i)\rangle \rightarrow |\Psi(J_\beta)\rangle$ photoionization cross section. The subscripts i, β, and f refer to the initial, intermediate, and final electronic states, respectively. $M^{\mu\nu}_{f\beta}$ in Eq. (1) is the Coulomb matrix element $\langle \psi_\mu(J_f)\epsilon_A l_A j_A; J_\beta \| \sum_{mn}^{N-1} 1/r_{mn} \| \psi_\nu(J_\beta)\rangle$. The Auger decay intensities were calculated using the AUGER component from the RATIP package. For more details about the AUGER program, see Refs. [32–34], and references therein.

IV. RESULTS AND DISCUSSIONS

The photoionization and the first step of the subsequent Auger decays of the K atom can be described as follows:

$$\begin{aligned} K + h\nu &\rightarrow K^+(2s^1) + e_p^-, \\ &\rightarrow \begin{cases} K^{2+}\,(2p^{-1}v^{-1}) + e_A^-\,(LLM,\ LLN) \\ K^{2+}\,(v^{-1}v^{-1}) + e_A^-\,(LMM,\ LMN) \end{cases}, \end{aligned} \quad (2)$$

where v represents the valence 3*s*, 3*p*, and 4*s* shells.

The first emitted electron is the photoelectron released from the 2*s* inner shell. After photoionization, the electronic transition in the K^+ ion leads to emission of an Auger electron e_A^-. The obtained K^{2+} $(2p^{-1}v^{-1})$ and K^{2+} $(v^{-1}v^{-1})$ states thus formed can further decay in a cascade process by emission of further Auger electrons, leading to K^{3+}, K^{4+}, K^{5+} or even possibly K^{6+} final states. This is because the ionization thresholds of K^{3+} (81.77 eV), K^{4+} (142.69 eV), K^{5+} (225.35 eV), and K^{6+} (324.79 eV) [35] are below the 2*s* ionization threshold that we measure at 385.3 eV (see below).Thus the decay path following the K 2*s* photoionization may lead energetically up to five Auger steps, although we experimentally observed only up to four coincident Auger events and failed to detect decay to K^{6+} states. Note that, in addition, the shake type of process may lead to the promotion of the outer 4*s* electron to the 5*s* or 6*s* shell during any of the steps in the path. The mixing of the 3*d* type orbitals is also observed and predicted by the calculations. This is often referred to as the "3*d* orbital collapse" [36].

A. 2*s* photoelectron spectrum

The experimental 2*s* photoionization spectrum presented in Fig. 1 shows a wide, strong peak found at a binding energy of 385.3 ± 0.2 eV and a less prominent structure at around 391.6 ± 0.2 eV. Fitting the spectrum with superposition of two components using the SPANCF curve fitting macro package developed by Kukk *et al.* [37] revealed Lorentzian linewidths of 2.6 eV ± 0.2 eV and 2.3 eV ± 0.3 eV for the main and satellite lines, respectively. A Gaussian linewidth of 1.2 eV was used to reflect the experimental resolution. The SPANCF

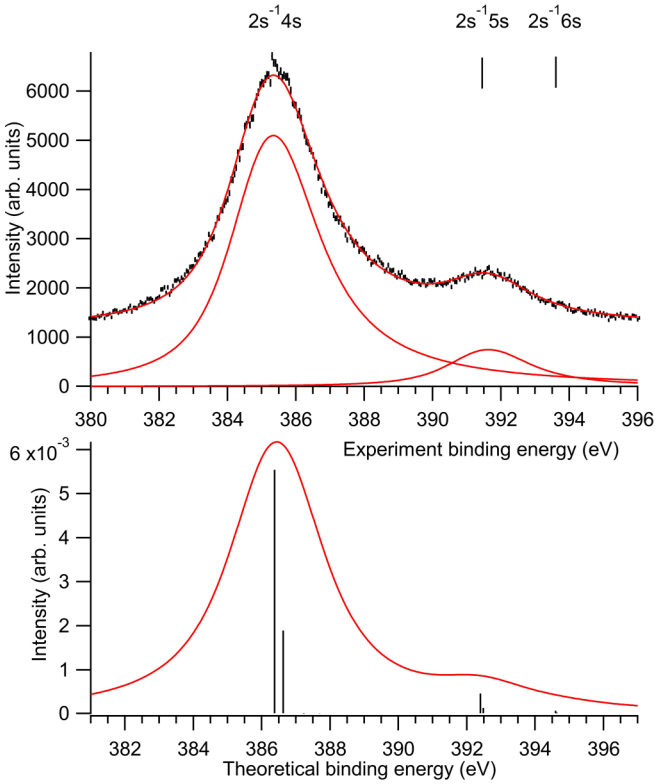

FIG. 1. K 2*s* photoionization spectrum measured at 460 eV photon energy corresponding to an excess energy of 74.7 eV (top) and the corresponding theoretical prediction (bottom). Prediction includes energies and intensities of the transitions (bars) and convoluted line profile to match the experiment. On top, experiment data points are fitted with a procedure including PCI distortion [37]. For the fitting procedure a 1.2 eV Gaussian contribution was used, reflecting the experimental resolution for electrons of ∼75 eV. The fitting procedure gave an estimation of 2*s* binding energy and lifetime; see text.

fitting procedure includes the PCI (Post Collision Interaction) distortion, as the 2*s* photoelectron of around 75 eV kinetic energy is followed by two Auger electrons: the first with ∼50 eV and the second with ∼200 eV. This kind of PCI due to the second Auger electron is known and was studied, for example, in Ref. [38].

This observed linewidth is slightly larger than the lifetime broadening $\Gamma = 2.25 \pm 0.5$ eV of the corresponding peak in the Ar 2*s* photoelectron spectrum [16]. This may be attributed to the increased number of Auger channels in K due to the presence of the additional 4*s* electron. To interpret the spectrum, the K 2*s* photoelectron transition was modeled with the MCDF method. For the ground state of K, a single configuration approach was used. To describe the singly ionized K $2s^1$ state, the MC calculations included a basis set consisting of nonrelativistic configurations $1s^2\,2s^1\,2p^6\,3s^2\,3p^6\,ns^1$ ($n = 4-6$) and $1s^2\,2s^1\,2p^6\,3s^2\,3p^6\,3d$. These calculations gave the ionization energies of 386.37 and 386.63 eV for the $2s^1$ (^1S) and (^3S) states, respectively. Thus, the predicted energy difference of the states is $\Delta E = 260$ meV, which cannot be resolved in the experiment. According to our calculations, the weaker structure observed at a binding energy of 392.4 eV originates from the transition from the K ground state to the $2s^15s$ satellite states. The transition probability to the next $2s^16s$ is so weak that it cannot be extracted from the background in our experiment.

The linewidths for the $2s^14s$ (^1S) and (^3S) states were calculated by using the nonrelativistic configurations $2s^2\,2p^5\,3s^1\,3p^6(3d, 4s, 5s, 6s)^1$, $2s^2\,2p^5\,3s^2\,3p^5(3d, 4s, 5s, 6s)^1$, $2s^2\,2p^5\,3s^2\,3p^4\,3d^1(4s, 5s, 6s)^1$, $2s^2\,2p^5\,3s^2\,3p^4\,4s^1(5s, 6s)^1$, $2s^2\,2p^5\,3s^2\,3p^4\,5s^1\,6s^1$, and $(3s, 3p)^6(4s, 3d, 5s)^1$, $(3s, 3p)^5\,3d^1(4s, 5s)^1$, $3s^2 3\,p^5$, and $3s^1\,3p^6$. The wave functions were first computed using these basis sets without configurations including the 5*s* and 6*s* orbitals. In the second step, the 5*s* and 6*s* radial wave functions were calculated using the full basis set while keeping the other wave functions fixed. The obtained linewidths for the $2s^14s$ (^1S) and (^3S) states are 2.84 and 2.87 eV, and 2.83 and 2.85 eV for the $2s^15s$ (^1S) and (^3S) states, respectively. This is consistent with the experimental finding that they are wider than the linewidth of the Ar 2*s* photoionization of 2.25 eV. The prediction also seems to slightly exceed the observed linewidth of 2.6 eV.

B. Auger decay of 2*s* vacancy

1. Overview of the Auger decay of K 2*s* vacancy

The complete K 2*s* coincident Auger spectrum is presented in Fig. 2. It is obtained by the histogram of all electrons detected in coincidence with a 2*s* photoelectron. In the low energy region between ∼20 and 75 eV, $L_1L_{2,3}M(N)$ Coster-Kronig lines are observed. Transitions $L_1MM(N)$ are observed at energies above 250 eV kinetic energy and are partially overlapped by Auger cascade transitions. The spectrum appears complex due to the overlapping of multiple decay paths, with the most intense one being the second step $L_{2,3}M$-MMM Auger lines present in the peak at 220 eV.

Compared to the Ar 2*s* case (Fig. 1 in Ref. [20]), the complete Auger spectrum shows similarities but also noticeable differences. Extra peaks appear due to the presence of the single 4*s* electron, resulting in lines such as $L_1L_{2,3}N$ and L_1MN. Additionally, sharp peaks at low kinetic energy are observed due to the emission of the 4*s* outer electron in further decay steps. It should be noted that the width of the Auger transitions corresponds to 2*s* lifetime broadening, which is estimated in this experiment to be 2.8 eV for the first step of the cascades. The Auger emissions in further steps of the decay path exhibit different widths depending on initial and final state effects specific to each transition.

2. Final K^{n+} populations reached by the decay of the K 2*s* vacancy

Auger spectra of the decay of the K 2*s* vacancy, involving one, two, three, and four Auger electrons, are presented in Fig. 3 and compared to corresponding spectra of Ar [20]. These spectra were obtained from coincidence events that involved one to four electrons detected in coincidence with a 2*s* photoelectron. They have been plotted as a function of the total kinetic energy of the Auger electrons. The structure of the spectra reveals the K^{n+} states populated by the Auger decays. According to the model described in [29], taking into account the estimated electron detection efficiency (∼65%), it

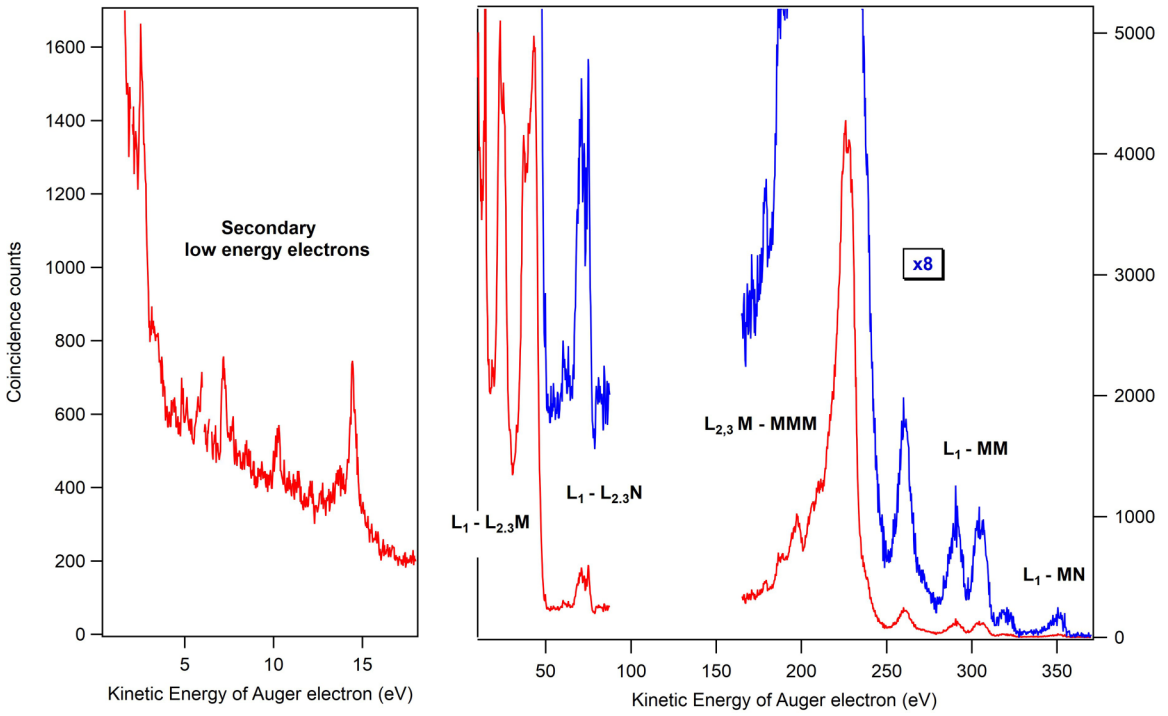

FIG. 2. The complete spectrum of all Auger electrons associated with the decay of the K 2*s* vacancy obtained by considering all electrons detected in coincidence with a 2*s* photoelectron. The measurement was carried out at 460 eV photon energy. Right: 300 meV discretization step. Left: 30 meV discretization step to reveal sharp, low energy lines. The observation of electrons in the range of 80–150 eV was prevented due to spurious weak true coincidences of 2*p* and 2*p* satellite lines with associated Auger lines that are emitted in the Ar 2*s* kinetic energy range.

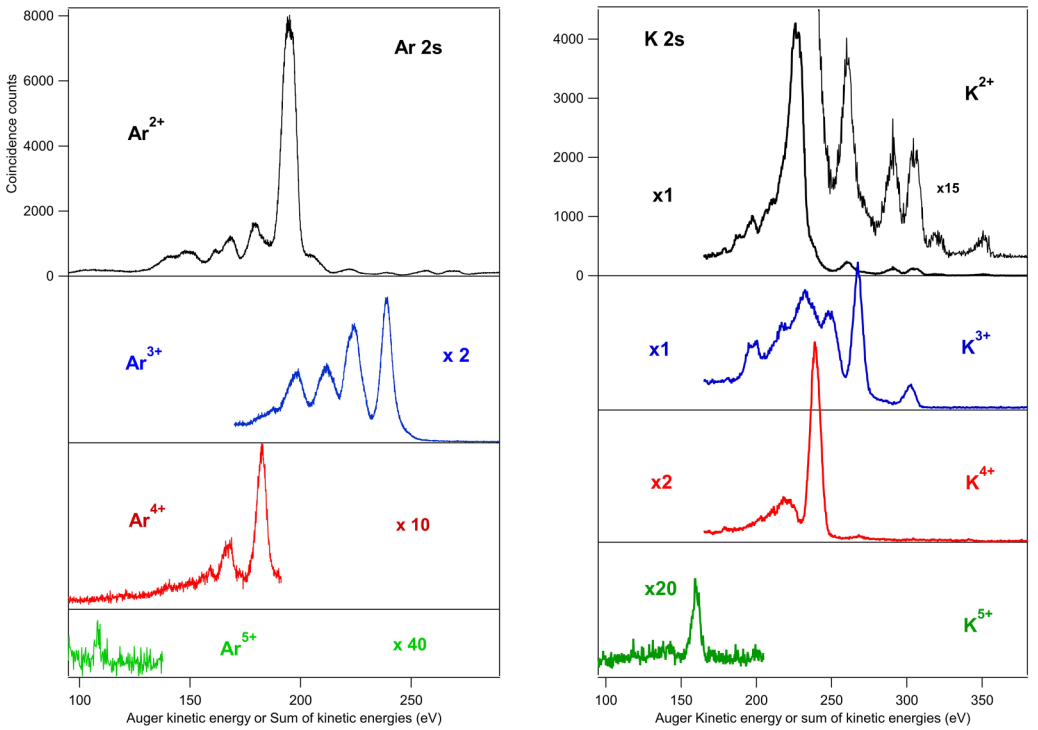

FIG. 3. Auger spectra of decay of the Ar 2*s* (left) and K 2*s* (right) vacancies involving one, two, three, and four Auger electrons, represented as a function of the total kinetic energy of the Auger electron(s). These spectra were obtained from coincidence events that involved detection of two, three, four or five electrons, where the 2*s* photoelectron was detected in coincidence with –one to four other electrons. Intensities correspond to the raw coincidence counts and have not been corrected here by detection efficiencies. The histograms are generated by plotting the sum of the kinetic energy of the Auger electrons.

TABLE I. Relative abundances of multiply charged K^{n+} and Ar^{n+} ions [20] produced by deexcitation of the K 2*s* and Ar 2*s* holes. Values are given in percentages (%).

Final ionic charge	K 2*s* Auger	Ar 2*s* Auger
+2	0.5	3
+3	56	89
+4	42	8
+5	1	0.3

is possible to extract from this data the probability of Auger electron cascade processes involving *n* Auger electrons. The overall comparison of the populations ending up in K^{n+} and Ar^{n+} ionic states after the completion of the Auger cascade process is shown in Table I. Values for Ar^{n+} populations are given in Ref. [20]. It is observed that a significantly larger portion of the Auger cascades ends up populating quadruply charged ionic states in K compared to Ar, where the major portion of Auger cascades end up in Ar^{3+} final states [20]. This larger final ionization degree in the case of K compared to Ar is due to the presence of the additional 4*s* electron in K, which is easily ejected.

The energy levels of the K^+, K^{2+}, K^{3+}, K^{4+}, and K^{5+} states are presented in Fig. 4. All levels in the diagram are referenced relative to the energy of the K $3p^6\,4s^1\ (^2S)$ ground state. The energy levels of the K^+ and K^{2+} states are calculated by us while K^{4+} and K^{5+} are referenced from the NIST Atomic Spectra Database [35]. K^{3+} levels include both calculated values and literature values taken from NIST for comparison and verification of the accuracy of our calculated K^{3+} energy values. The calculations for the K^{3+} energy levels utilized the configurations of $(3s\,3p)^5(3d\,4s\,5s)^1$, $(3s\,3p)^4\,3d^1\,(4s\,5s)^1$, and $(3s\,3p)^6$. K^{3+} states with a major contributing electron configuration of $(3s\,3p)^4\,3d^1\,(4s\,5s)^1$ are not presented in Fig. 4 to enhance the clarity of the displayed states.

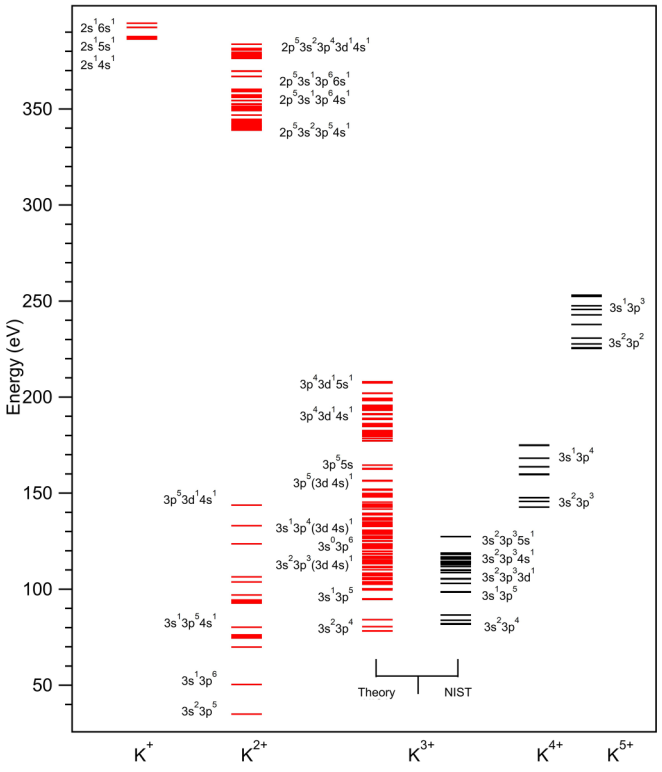

FIG. 4. A schematic energy level diagram illustrating the energies of the K^+, K^{2+}, and K^{3+} states of interest. The energy levels are referenced relative to the K $3p^64s\ (^2S)$ ground state. Each horizontal line in the diagram represents an individual state, and the major electronic configurations are schematically labeled. The energy level values for K^+ and K^{2+} are calculated (red lines), while the energy level values for K^{4+} and K^{5+} are obtained from the NIST database (black lines) [35]. K^{3+} levels include both calculated values (red lines) and references from NIST (black lines). Only notably populated K^{2+} states are included in the figure.

3. L_1MN and L_1MM Auger decays

Let us first study the valence Auger transitions, in which the decay of the 2*s* hole implies two valence electrons from the 4*s*, 3*s*, or 3*p* orbitals. Figure 5 deals with the associated L_1MN and L_1MM Auger lines. Figure 5(b) shows the part of the complete experimental Auger spectrum of Fig. 2, where these Auger lines appear. The spectrum is plotted as a function of the Auger kinetic energy (E_k) and also of the energy of the K^{2+} final state (E_b), using the relation: $E_b = E_b(2s) - E_k$, where $E_b(2s)$ presents the binding energy of the 2*s* hole.

In the theoretical prediction, shown at the top [Fig. 5(a)], only the decay through the L_1MN and L_1MM transitions to the lowest energy double ionized states is presented. The MC calculations for the valence final states included nonrelativistic configurations $(3s, 3p)^6(4s, 3d, 5s)^1$, $(3s, 3p)^5\,3d^1(4s, 5s)^1$, $3s^2 3\,p^5$, and $3s^1\,3p^6$. The calculated energies and intensities are convoluted with a Voigt profile [red line in Fig. 5(a)], using a Lorentzian linewidth of 2.4 eV and a Gaussian linewidth of 4 eV, to simulate the experimental results. This prediction aligns well with the experimental results below 100 eV energies. The lowest state $3s^2 3\,p^5$ is clearly observed in both theory and experiment. At around 60 eV energy, the theory predicts intensity for the transition to the $3s^1\,3p^6$ double ionized states, while the experiment obviously shows more intensity transferred to the $3s^2 3\,p^4 4\,s^1$ states. On the opposite, the two large peaks at energy around 90 eV agree in both theory and experiment and are assigned to the $3s^1 3\,p^5 4\,s^1$ group of states.

It is noteworthy that the energy of the lowest K^{3+} state is 81.7 eV [35]. Therefore, all the populated double ionized states above this energy decay through the second step Auger process. This is clearly observed in Fig. 5(c), which represents the $e - e$ coincidence spectrum between two Auger electrons, with the additional selection of the K 2*s* photoelectron. The final triply ionized states form diagonal lines with defined structures, representing the two observed Auger electrons sharing the available energy. The projection on the left *y* axis of the rightmost diagonal line [Fig. 5(d)] reflects the formation of the K^{3+} $3s^2\,3p^4$ states, for which $E_{k1} + E_{k2}$ is approximately 302 eV (where E_{ki} is kinetic energy of the *i*th Auger electron).

In Fig. 5(d), the *y* projection clearly shows sharp lines between 0 and 13 eV, resulting from the release of the 4*s* outer

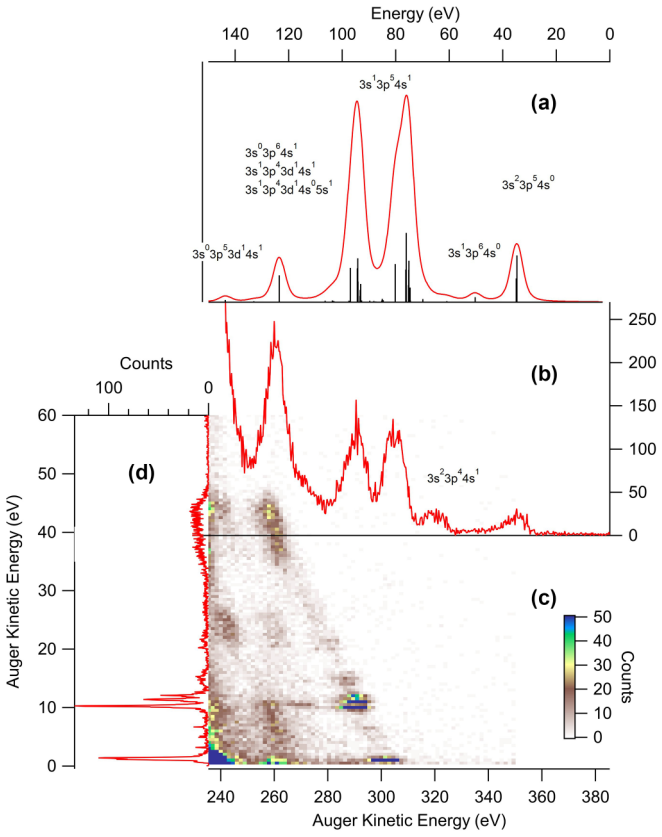

FIG. 5. L_1MN and L_1MM decay. (a) Theoretical K $2s$ Auger spectrum associated with decay to K^{2+} valence states. The calculations are represented by bars and convoluted with a Voigt profile (red line) to simulate experimental data. The energies are referenced relative to the K $3p^6 4s$ ground state. (b) Experimental data, representing the complete Auger spectrum in this energy region, from Fig. 2. (c) Auger-Auger coincidence map obtained through three electron coincidences (the $2s$ photoelectron and two Auger electrons). A linear scale is used for the color encoding. (d) Projection of the intensity on the rightmost diagonal line, corresponding to the formation of the K^{3+} $3s^2\,3p^4$ ground states, defined by a sum of the kinetic energies of the two Auger electrons in the 295–310 eV band.

electron in the last step of the Auger decay, according to the following process:

$$L_1M_1M_{2,3}\,2s^1 \rightarrow K^{2+}(3s^1 3p^{-1} 4s^1) + e_{A1}(\sim 290\,\text{eV}),$$
$$M_{2,3}M_{2,3}N \rightarrow K^{3+}(3p^{-2} 4s^0) + e_{A2}(\sim 0\,\text{to}\,13\,\text{eV}), \quad (3)$$

Additionally, a broad band around 40 eV is observed in Fig. 5(d), associated with an Auger electron with a kinetic energy of ∼260 eV. The broadness of the 40 eV band, in contrast to the sharpness of the lower energy lines, suggests that the 40 eV electrons are emitted in the first step of the Auger cascade. The process involved is as follows:

$$L_1L_{2,3}M_{2,3}\,2s^1 \rightarrow K^{2+}(2p^{-1} 3p^1 4s^1) + e_{A1}\,(\sim 40\,\text{eV}),$$
$$M_{2,3}M_{2,3}N \rightarrow K^{3+}(3p^{-2} 4s^0) + e_{A2}\,(\sim 260\,\text{eV}). \quad (4)$$

This process corresponds to a Coster-Kronig transition in the first step. Thus, in the current experiment, the order of the electron ejection can be inferred. In the first case [Eq (3)], emission of a high kinetic energy electron is followed by a slow (sharp) transition, while in the latter case [Eq. (4)], the first, low kinetic energy electron belongs to a rapid (broad) Coster-Kronig transition. Due to the selection of configurations in the MC calculation (only valence transitions), the Coster-Kronig channels are not included in the prediction of Fig. 5(a), explaining the difference between theory and experiment.

The calculated spectrum in Fig. 5(a) is dominated by the K^{2+} $3s^1\,3p^{-1}$ configuration. The $3p^{-1}4s^1$ and $3s^1\,4s^1$ configurations are also clearly observable. This is consistent with Ar [20], as the transitions to $3s^1\,3p^{-1}$ are the most intense ones. The state predicted at around 123 eV energy is highly mixed, consisting of $3s^0\,3p^6\,4s^1$, $3s^1\,3p^4\,3d^1\,4s^1$, and $3s^1\,3p^4\,3d^1\,4s^0\,5s^1$ configurations. Its experimental observation is complicated due to the superposition of the Coster-Kronig channel mentioned above [Eq. (4)]. However, it can tentatively be assigned to the coincident structure seen at (270 eV, 10 eV) in Fig. 5(c), suggesting that the decay of this mixed $3s^0\,3p^6\,4s^1$ states occurs to the excited K^{3+} $3s^1\,3p^5$ final state, according to the following reaction:

$$L_1M_1M_1\,2s^1 \rightarrow K^{2+}(3s^{-2}) + e_{A1}\,(\sim 270\,\text{eV}),$$
$$M_1M_{2,3}N \rightarrow K^{3+}(3s^1 3p^{-1} 4s^1) + e_{A2}\,(\sim 10\,\text{eV}). \quad (5)$$

The involvement of the $3d$ orbital is a typical signature of the "$3d$ collapse," i.e., readaptation of the orbital to the charge of the core electron configuration ($2s^1$). The transitions to the K^{2+} final states involving the emission of the $4s$ electron ($3s^2 3\,p^5$ and $3s^1\,3p^6$) are naturally unique to the K case due to the presence of the $4s$ electron. The state $3s^0\,3p^5\,3d^1\,4s^1$ is predicted to obtain intensity but is challenging to distinguish experimentally from the population through the Coster-Kronig channel.

As a summary, based on our observations, in the single Auger decay to final K^{2+} states, the outer $4s$ electron is preferentially a spectator, populating the $3s^2 3\,p^4 4\,s^1$ and low energy $3s^1 3\,p^5 4\,s^1$ levels. However, in approximately 30% of the cases, the $4s$ electron can also participate, populating the K^{2+} $3s^2 3\,p^5$ states.

4. $L_1L_{2,3}M$ and $L_1L_{2,3}N$ decays: Spectroscopy of intermediate K^{2+} $2p^{-1}v^{-1}$ core-valence states revealed beyond the lifetime broadening

The Coster-Kronig path involving the $2p$ level [as written in the second line of Eq. (2)] is recognized as the dominant decay mechanism for the $2s$ hole. The corresponding $K^{2+}2p^{-1}v^{-1}$ states, reached through this pathway, are revealed in the kinetic energy range of ∼20–75 eV in the $2s$ Auger spectrum in Fig. 2. However, the broadening of the peaks caused by the $2s$ lifetime prevents a detailed identification of these K^{2+} states. To overcome this limitation, the multielectron coincidence experiment offers a unique opportunity to resolve states that extend beyond the natural widths of the transitions. This approach has been described in Refs. [19,39], and is demonstrated in the two-dimensional (2D) plot presented in Fig. 6(a). The figure displays electron-electron coincidences between the $L_1L_{2,3}M$ (N) Auger lines (vertical axis) and the faster photoelectron (horizontal axis), considering coincidence events involving the detection of three electrons: the two mentioned above and a third electron

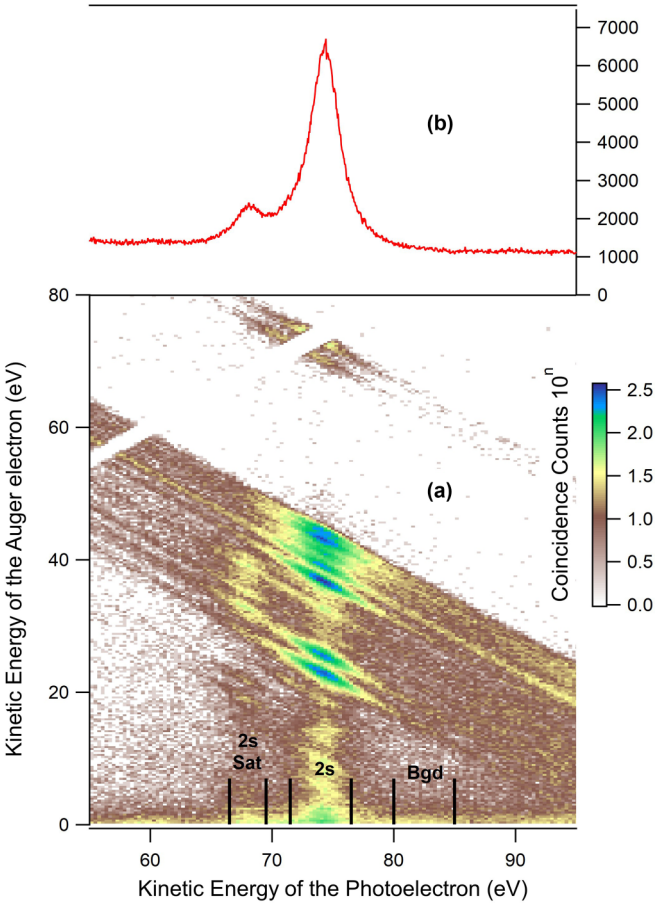

FIG. 6. Decay of $2s$ and $2s$ satellite to K^{2+} $2p^{-1}v^{-1}$ states. (a) 2D map of electron-electron coincidences when the electron pair is detected with a third electron of $200-250$ eV, corresponding to the energy range of the Auger electron emitted in the last step of the cascade decay. A log scale is used for the color encoding. The diagonal line on the top left corner, with no coincidence counts, corresponds to the blind zone where our experiment is unable to detect electrons of too close energies. The three zones ($2s$ Sat, $2s$, and Bgd) indicate the ranges used to extract the signal from the $2s$ satellite, from the $2s$, and to estimate the background. In (b) the red curve represents the projection of the 2D map onto the x axis, displaying the peaks of the $2s$ photoelectron. It is similar to the noncoincidence photoelectron spectrum of Fig. 1.

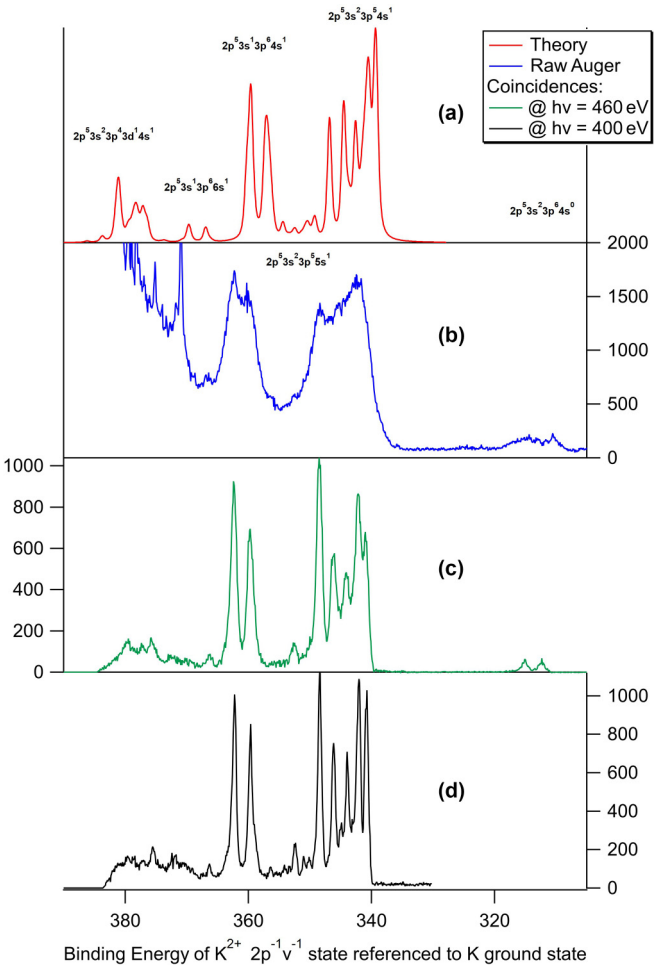

FIG. 7. $L_1L_{2,3}M$ and $L_1L_{2,3}N$ Coster-Kronig decays. (b) The conventional $2s$ Auger spectrum is broadened by the 2.6 eV lifetime broadening of the $2s$ hole. The experimental spectra (b)–(d) and calculated spectrum (a) represent the overall contribution of the decay of the K $2s$ main states to final states with $2p^{-1}v^{-1}$ configurations. Coincidence spectroscopy allows for the detection of populations with resolution beyond natural lifetime broadening, as demonstrated in (c,d). The energies are referenced relative to the K $3p^6 4s$ ground state.

with an energy range of $200-250$ eV, corresponding to the second step Auger process. The projection of the coincidence map onto the x axis reproduces the $2s$ photoelectron spectrum, depicted as a red curve in Fig. 6(b).

The diagonal structures in the two-dimensional coincidence map correspond to the K^{2+} $(2p^{-1}v^{-1})$ core-valence states. As indicated in Eq. (2), the total kinetic energy of the two electrons is given by $E_{\text{tot}} = E_1 + E_2 = h\nu - E(K^{2+})$, which is perceived as several diagonal structures in the 2D coincidence map. Therefore, each of these diagonal structures corresponds to the population of a certain K^{2+} $(2p^{-1}v^{-1})$ core-valence state. These core-valence states are found to be populated differently by the decay of the $2s$ hole, the $2s$ satellite hole, and also outside of these "resonances," due to a direct core-valence double photoionization path. The diagonal population of these doubly ionized states, resulting from the decay of the $2s$ hole, is presented in Fig. 7(c). The signal has been selected within the "$2s$" zone in Fig. 6(a), while subtracting a background estimated in the "Bgd" zone. Figure 7 provides a comparison of the spectroscopic information regarding the K^{2+} $(2p^{-1}v^{-1})$ core-valence state, as deduced from the conventional K $2s$ Auger spectrum [panel (b)] and from this "subnatural linewidth Auger-photoelectron coincidence spectroscopy" method [panels (c), (d)]. The improved resolution achieved by using a lower photon energy (and thus a slower photoelectron) is evident when comparing Fig. 7(d), measured with a photon energy of 400 eV, and Fig. 7(c), measured at 460 eV.

The double ionized K^{2+} $2p^{-1}v^{-1}$ states were modeled in Fig. 7(a) using the multiconfigurational approach with a basis that included nonrelativistic configurations $2s^2\,2p^5\,3s^1\,3p^6(3d, 4s, 5s, 6s)^1$, $2s^2\,2p^5\,3s^2 3p^5(3d, 4s, 5s, 6s)^1$, $2s^2\,2p^5$

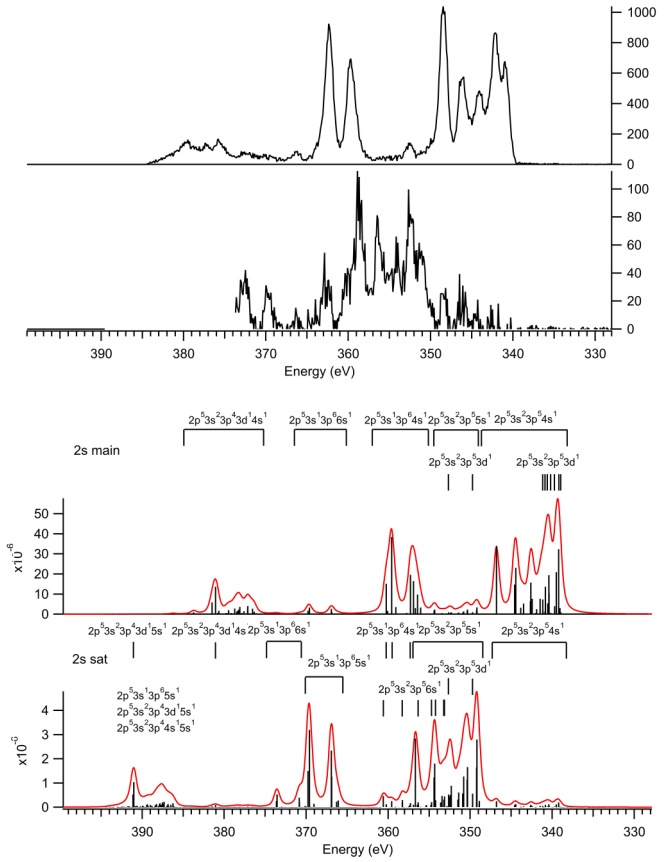

FIG. 8. L_1LM: Experimental (top) and calculated (bottom) populations of the K^{2+} $2p^{-1}v^{-1}$ core-valence states populated by the decay of K 2*s* main and satellite states. The energies are referenced relative to the K $3p^6 4s$ ground state.

$3s^2\,3p^4\,3d^1(4s, 5s, 6s)^1$, $2s^2 2p^5\,3s^2\,3p^4\,4s^1(5s, 6s)^1$, and $2s^2\,2p^5\,3s^2\,3p^4\,5s^1\,6s^1$. The calculations were initially performed without the 5*s* and 6*s* orbitals. In the second step, the 5*s* and 6*s* radial wave functions were calculated upon these while keeping either of the 5*s* or 6*s* and the wave functions obtained in the first step of the calculation fixed. Agreement between our calculations [Fig. 7(a)] and our measurements [Figs. 7(c) and 7(d)] is excellent.

a. Comparison of the formation of K^{2+} $2p^{-1}v^{-1}$ *core-valence states by decay of the 2s and 2s satellite vacancies.* Experimental and calculated core-valence states of K^{2+} $2p^{-1}v^{-1}$ populated by 2*s* hole decay are shown in Fig. 7 and compared to contributions from 2*s* satellite lines in Fig. 8. Good agreement is observed between the experimental and theoretical spectra. The predicted energy shows an offset of approximately 1.5–2.5 eV, which is typical for this type of calculation. For the 2*s* satellite, the main peaks appear to be shifted towards higher energies compared to the 2*s* decay, possibly because the final states are $2p^{-1}3p^{-1}5s$ instead of $2p^{-1}3p^{-1}4s$, as in the case of 2*s* decay.

Both the theoretical and experimental spectra show that the transition from initial states $2s^1 4s$ populates mainly $2s^2\,2p^5\,3s^2\,3p^5\,4s^1$ and $2s^2\,2p^5\,3s^1\,3p^6\,4s^1$ final states. In the case of the 2*s* satellite, the main peaks appear to be shifted towards higher energies as the transitions from the $2s^1 5s$

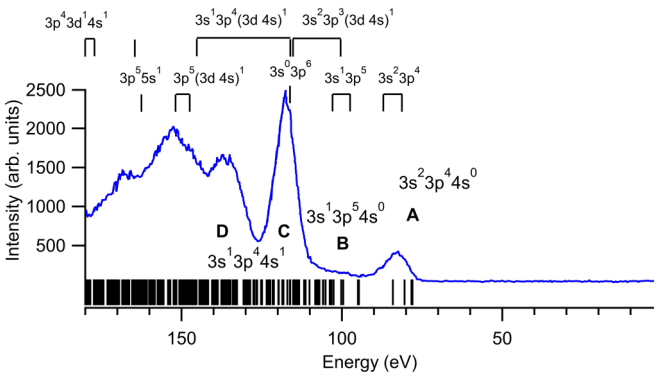

FIG. 9. K^{3+} states populated by double Auger decay of the K 2*s* vacancy, from Fig. 3, together with calculated K^{3+} energy levels (black bars) and major contributing configurations. The energies are referenced relative to the K $3p^6 4s$ ground state.

satellite states populate primarily $2s^2\,2p^5\,3s^2\,3p^5\,5s^1$ final states, as confirmed by our calculations. However, regardless of whether the initial state is $2s^1 4s$ or $2s^1 5s$, the populations of the K^{2+} states by the 2*s* hole decay are very similar. It does not significantly affect the overall shape of the spectrum, as the outer electron remains a spectator in the process, clearly seen in Fig. 8. This similarity is also evident in the comparison with Ar 2*s* vacancy decay, where aside from minor additional structures caused by spin-orbit splitting, the overall structure of the spectrum is also very similar to the Ar case [20].

The calculated shakedown probability from $2s^1 5s$ states is approximately 14%. On the other hand, in the Auger decay of the K 3*s* hole, the outer electron actively participates in the decay process, leading to the predominant population of $3p^5\,4s^1$ states, which is clearly different compared to decay of the K 2*s* hole [22].

5. Cascade decays of the K 2s vacancy to K^{3+} *final states by emission of two Auger electrons*

In Sec. IV B we observed that L_1MN valence Auger transitions end up in K^{2+} final states, while L_1MM valence Auger transitions often initiate cascade decays to K^{3+} final states, in which the outer 4*s* electron is ejected in the final step of the cascade. Now let us investigate the main source of formation for K^{3+} final states, which occurs through $L_1L_{2,3}M$ Auger transitions. In Fig. 3, the decay of the 2*s* hole to K^{3+} states was analyzed by examining three electron coincidences involving the 2*s* photoelectron and the two subsequent Auger electrons. The spectrum of the K^{3+} states was represented as a function of the sum of the kinetic energies of these two Auger electrons, $E_{A1} + E_{A2}$. Figure 9 represents this spectrum as a function of the energy $E_b(K^{3+})$ of the K^{3+} states, as obtained from

$$E_b(K^{3+}) = E_b(2s) - (E_{A1} + E_{A2}). \tag{6}$$

The energy levels of the K^{3+} states were calculated to aid in the interpretation of the experimental spectrum. Calculations

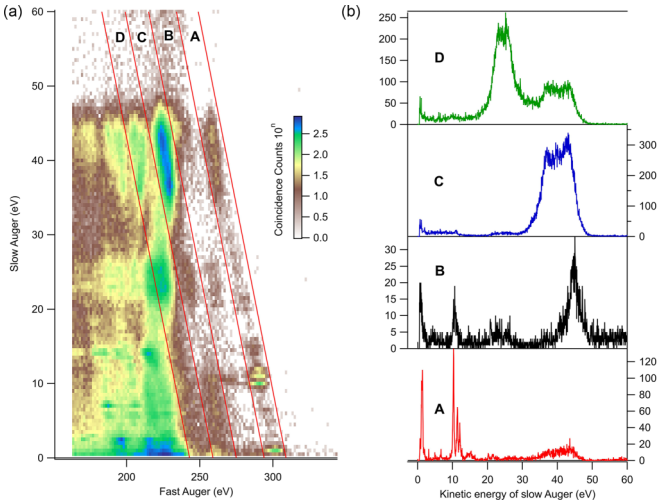

FIG. 10. Double Auger decay of the K 2*s* vacancy. (a) An Auger-Auger coincidence map as obtained by three electron coincidences (the 2*s* photoelectron and the two Auger electrons). A logarithmic scale is used for color encoding. (b) Spectra of low energy Auger electrons released in the double Auger decay to the indicated K^{3+} final states.

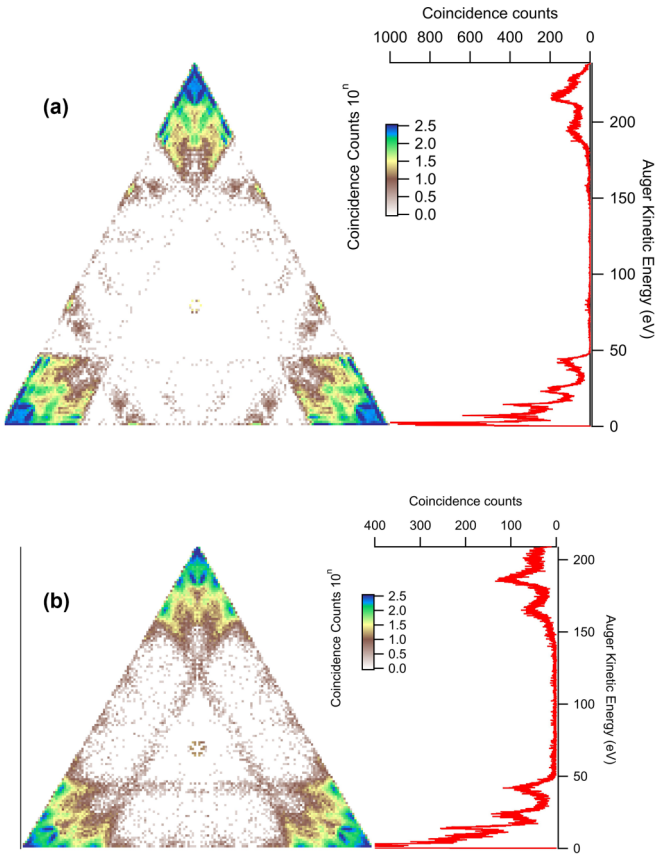

FIG. 11. Dalitz plots depicting the energy correlation between the three subsequent K 2*s* Auger electrons emitted during decay to K^{4+} "ground" (a) and to K^{4+} "excited" states (b). On the right: projections of the triangles on the vertical axis, displaying the energy distribution of any emitted Auger electrons.

were performed using configurations $(3s\,3p)^5(3d\,4s\,5s)^1$, $(3s\,3p)^4\,3d^1\,(4s\,5s)^1$, and $(3s\,3p)^6$. By comparing the experimental spectrum in Fig. 9 with the calculated values and literature references [35] for the energy levels of K^{3+} states, the assignment of stable final states for K^{3+} (which are below the K^{4+} threshold at 142.7 eV [35]) can be proposed. Based on this analysis, peak *A* corresponds to $3s^2\,3p^4$ states, peak *B* corresponds to $3s^1\,3p^5$ states, and *D* and *C* correspond to $3s^2\,3p^3\,(4s3d)^1$, $3s^0\,3p^6$, and $3s^1\,3p^4\,(3d4s)^1$ states.

The energy correlations between the two Auger electrons are shown in Fig. 10, which provides an extended view of Fig. 5(c). In this presentation, the K^{3+} states appear on diagonal lines with a fixed energy sum along the diagonal. On the right side of the figure is the projection on the *y* axis of the four zones in the electron-electron coincidence map, corresponding to the K^{3+} final states *A*–*D*, which were assigned in Fig. 9.

As discussed in Sec. IV B above, sharp lines in *A* and *B* in Fig. 10 indicate the ejection of the 4*s* electron in the final step of the cascade. However, for the more intensively populated *C* and *D* bands, a broad band prevails. *C* is mainly populated by the $L_1L_{2,3}M_{2,3}$ path, as shown by the low energy Auger band of approximately 40 eV. In the last step, a ∼240 eV Auger electron is emitted, resulting in the formation of the K^{3+} *C* state. This state can be described with mixed configurations where the 4*s* level is occupied. The situation is similar for the formation of K^{3+} *D* final states, except that the dominant path is now $L_1L_{2,3}M_1$, as shown by the low energy Auger band of around 25 eV. In the final step, a ∼235 eV Auger electron is emitted. In conclusion, in the double Auger decay process, the 4*s* electron is a spectator for most of the cascade process and remains in the final ion.

6. Cascade decays of the K 2s vacancy to K^{4+} final states by emission of three Auger electrons

In the cascade decays of the K 2*s* vacancy to K^{4+} final states, three Auger electrons are emitted, and it is possible to represent energy correlation between them using a Dalitz plot [29] if the sum of their kinetic energies E_S is fixed. Referring to the spectrum of the K^{4+} final states in Fig. 3, two distinct bands of K^{4+} states can be identified: the more intense band with $E_S = 240$ eV can be assigned to a $3s^2 3\,p^3$ configuration, while the weaker band with $E_S = 220$ eV is associated to a $3s^1 3\,p^4$ configuration. The corresponding Dalitz plots are represented in Fig. 11. Full explanations on Dalitz representation can be found in [29]. Briefly, the energy correlation between the three electrons appears in an equilateral triangle. Each point of the triangle represents a triplet of electrons, of kinetic energies given by the distances to the three sides of the triangle, giving rise to a highly symmetric figure. A noticeable property is that projection of the Dalitz plot on the vertical (symmetry) axis of the triangle gives the energy distribution of the three Auger electrons. It is represented on the right side of Fig. 11.

The decay process in K is clearly different compared to the decay of Ar 2*s* [29], due to the presence of the additional 4*s* electron. The probability for the 2*s* hole decay through the

emission of three Auger electrons in K was determined to be 42% (refer to Table I), which is over five times larger than in the case of Ar 2*s* triple Auger decay. In the Dalitz plots of Ar [29], it was observed that the last two Auger electrons emitted in the cascade are often emitted simultaneously, resulting in horizontal bands in the Dalitz plot. In K, only a faint occurrence of such a process is observed for decay to the excited K^{4+} state [Fig. 11(b)]. The dominant decay in K involves a three-step cascade process. In the first step, a Coster-Kronig Auger decay occurs, where the 2*s* hole is replaced by a 2*p* hole, leading to the appearance of two prominent bands at approximately 40 and 25 eV in the Auger spectrum (Fig. 11, right). Subsequently, in the second step, the 2*p* hole is filled, accompanied by the emission of an Auger electron with an energy of approximately 200 eV. This is the same path that has been observed previously (Sec. IV B) for decay through the emission of two Auger electrons to K^{3+} final states. However, in this case, the resulting K^{3+} states are excited states located above the K^{4+} threshold, and they decay by emitting a low energy, less than 20 eV, Auger electron. Calculations in Fig. 9 suggest that these high energy K^{3+} states maintain occupation of the 4*s* level. Consequently, we can deduce that the outer 4*s* electron remains as a spectator during the beginning of the Auger decay but is released in the final step of the three-step cascade to K^{4+} final states.

V. CONCLUSION

Photoionization from the K 2*s* subshell in initially neutral atomic potassium and the subsequent Auger decay cascade processes have been investigated using magnetic bottle multicoincidence spectroscopy with synchrotron radiation.

The decay paths following K 2*s* photoionization have been comprehensively described obtaining the population of the cascade K^{n+} ($n = 2 - 4$) final states. The experimental findings were compared with theoretical predictions obtained from the multiconfiguration Dirac-Fock (MCDF) approach, as well as previous observations of corresponding cascade processes in argon. These comparisons highlight differences attributed to the presence of an additional 4*s* electron.

In the 2*s* photoelectron spectrum, a prominent peak corresponds to the $2s^1$ (^1S) and (^3S) states. However, due to the small energy difference between these states (predicted $\Delta E =$ 260 meV), they cannot be resolved in the experiment. The experimental linewidth of the states is measured to be 2.6 eV $\pm$ 0.2 eV, which is slightly wider than the corresponding linewidth of Ar 2*s* ($\Gamma = 2.25 \pm 0.5$ eV) [16]). Additionally, the 2*s* photoelectron spectrum exhibits a weaker structure attributed, according to our calculations, to transitions to K $2s^1 5s$ satellite states. The transition probability to the next $2s^1 6s$ states is so weak that it cannot be extracted from the background in our experiment.

In the single Auger decay to final K^{2+} states, the outer 4*s* electron primarily acts as a spectator, populating the $3s^2 3p^4 4s^1$ and low energy $3s^1 3p^5 4s^1$ levels. However, in approximately 30% of the cases, the 4*s* electron can also participate, populating the K^{2+} $3s^2 3p^5$ states.

L_1MM valence Auger transitions often initiate cascade decays to K^{3+} final states, where the outer 4*s* electron is ejected in the final step of the cascade. However, the main source of formation for K^{3+} final states is the $L_1L_{2,3}M$ Coster-Kronig transitions. The broadening of the peaks caused by the 2*s* lifetime prevents a detailed identification of these K^{2+} states. To overcome this limitation, the multielectron coincidence experiment offers a unique opportunity to resolve states beyond the natural widths of transitions. Experimental and calculated K^{2+} $2p^{-1}v^{-1}$ core-valence states, populated by 2*s* hole decay, are shown and good agreement is observed between the experimental and theoretical spectra. In the double Auger decay process to the K^{3+} final states, the 4*s* electron acts as a spectator for most of the cascade process and remains in the final ion.

Dalitz plots were used to analyze the K 2*s* triple Auger decay to K^{4+} states. The experimental results have been compared to predictions obtained with the MCDF method, revealing good agreement between the experimental findings and theoretical calculations. In the Auger cascade processes, a notable observation is that a significantly larger portion of the Auger cascades lead to quadruply charged ionic states in potassium compared to argon. In contrast, a major portion of the Auger cascades in argon end up in Ar^{3+} final states [20]. This larger final ionization degree in the case of K compared to Ar arises from the presence of the additional 4*s* electron in K, which is easily ejected.

In general, notable differences have been observed, primarily attributed to the presence of an additional 4*s* electron above the closed shell electronic structure of rare gases. It has been observed that the outer 4*s* electron predominantly acts as a spectator during the Auger decay process and is eventually emitted in the final step of the Auger cascade. This study represents a continuation of research focused on obtaining fundamental information regarding the electronic structure and quantum mechanical transition processes in the potassium atom [22].

ACKNOWLEDGMENTS

This work has been financially supported by the Research Council of Finland. The Väisälä Foundation is acknowledged by S.-M.A. The Tauno Tönning Foundation is acknowledged by J.S. The experiments were performed at SOLEIL Synchrotron (France) at the PLEIADES beam line, with the approval of the Soleil Peer Review Committee (Projects No. 20120132 and No. 20131019). We are grateful to the PLEIADES team for their help during the measurements and to SOLEIL staff for stable operation of the storage ring.

[1] See, for, example, D. W. Turner and D. P. May, J. Chem. Phys. **45**, 471 (1966); D. W. Turner and W. C. Price, Proc. R. Soc. London, Ser. A **307**, 15 (1968).

[2] K. Siegbahn, *ESCA Atomic, Molecular and Solid-State Structure Studied by Means of Electron Spectroscopy*, Nova Acta Regiae Societis Scientiarum Upsaliensis, Series IV, Vol. 20 (Almqvist & Wiksell Boktryckeri AB, Uppsala, 1967).

[3] D. Castelvecchi, Nature (London) **525**, 7567 (2015).
[4] M. Braune, A. Reinköster, J. Viefhaus, S. Korica, and U. Becker, J. Phys.: Conf. Ser. **194**, 032016 (2009).
[5] J. H. D. Eland, O. Vieuxmaire, T. Kinugawa, P. Lablanquie, R. I. Hall, and F. Penent, Phys. Rev. Lett. **90**, 053003 (2003).
[6] M. Huttula, S.-M. Huttula, P. Lablanquie, J. Palaudoux, L. Andric, J. H. D. Eland, and F. Penent, Phys. Rev. A **83**, 032510 (2011).
[7] M. A. Khalal, J. Soronen, K. Jänkälä, S.-M. Huttula, M. Huttula, J.-M. Bizau, D. Cubaynes, S. Guilbaud, K. Ito, L. Andric, J. Feng, P. Lablanquie, J. Palaudoux, and F. Penent, J. Phys. B: At. Mol. Opt. Phys. **50**, 225003 (2017).
[8] R. Feifel, J. H. D. Eland, R. J. Squibb, M. Mucke, S. Zagorodskikh, P. Linusson, F. Tarantelli, P. Kolorenč, and V. Averbukh, Phys. Rev. Lett. **116**, 073001 (2016).
[9] M. Huttula, S.-M. Huttula, S. Fritzsche, P. Lablanquie, F. Penent, J. Palaudoux, and L. Andric, Phys. Rev. A **89**, 013411 (2014).
[10] P. Lablanquie, F. Penent, and Y. Hikosaka, J. Phys. B: At. Mol. Opt. Phys. **49**, 182002 (2016).
[11] Y. Hikosaka, M. Fushitani, A. Matsuda, C.-M. Tseng, A. Hishikawa, E. Shigemasa, M. Nagasono, K. Tono, T. Togashi, H. Ohashi, H. Kimura, Y. Senba, M. Yabashi, and T. Ishikawa, Phys. Rev. Lett. **105**, 133001 (2010).
[12] P. Lablanquie, F. Penent, J. Palaudoux, L. Andric, P. Selles, S. Carniato, K. Bucar, M. Zitnik, M. Huttula, J. H. D. Eland, E. Shigemasa, K. Soejima, Y. Hikosaka, I. H. Suzuki, M. Nakano, and K. Ito, Phys. Rev. Lett. **106**, 063003 (2011).
[13] L. J. Frasinski, V. Zhaunerchyk, M. Mucke, R. J. Squibb, M. Siano, J. H. D. Eland, P. Linusson, P. v.d. Meulen, P. Salén, R. D. Thomas, M. Larsson, L. Foucar, J. Ullrich, K. Motomura, S. Mondal, K. Ueda, T. Osipov, L. Fang, B. F. Murphy, N. Berrah *et al.*, Phys. Rev. Lett. **111**, 073002 (2013).
[14] K. Jänkälä, P. Lablanquie, F. Penent, J. Palaudoux, L. Andric, and M. Huttula, Phys. Rev. Lett. **112**, 143005 (2014).
[15] S. Zhong, J. Vinbladh, D. Busto, R. J. Squibb, M. Isinger, L. Neoričić, H. Laurell, R. Weissenbilder, C. L. Arnold, R. Feifel, J. M. Dahlström, G. Wendin, M. Gisselbrecht, E. Lindroth, and A. L'Huillier, Nat. Commun. **11**, 5042 (2020).
[16] P. Glans, R. E. La Villa, M. Ohno, S. Svensson, G. Bray, N. Wassdahl, and J. Nordgren, Phys. Rev. A **47**, 1539 (1993).
[17] W. Mehlhorn, Z. Phys. **208**, 1 (1968).
[18] T. Kylli, J. Karvonen, H. Aksela, A. Kivimäki, S. Aksela, R. Camilloni, L. Avaldi, M. Coreno, M. de Simone, R. Richter, K. C. Prince, and S. Stranges, Phys. Rev. A **59**, 4071 (1999).
[19] P. Lablanquie, F. Penent, R. I. Hall, H. Kjeldsen, J. H. D. Eland, A. Muehleisen, P. Pelicon, Z. Smit, M. Zitnik, and F. Koike, Phys. Rev. Lett. **84**, 47 (2000).
[20] P. Lablanquie, S.-M. Huttula, M. Huttula, L. Andric, J. Palaudoux, J. H. D. Eland, Y. Hikosaka, E. Shigemasa, K. Ito, and F. Penent, Phys. Chem. Chem. Phys. **13**, 18355 (2011).
[21] L. Avaldi, J. J. Jureta, and B. P. Marinković, J. Electron Spectrosc. Relat. Phenom. **237**, 146898 (2019).
[22] J. Palaudoux, S. Sheinerman, J. Soronen, S.-M. Huttula, M. Huttula, K. Jänkälä, L. Andric, K. Ito, P. Lablanquie, F. Penent, J-M. Bizau, S. Guilbaud, and D. Cubaynes, Phys. Rev. A **92**, 012510 (2015).
[23] M. Koide, F. Koike, Y. Azuma, and T. Nagata, J. Electron Spectrosc. Relat. Phenom. **144–147**, 55 (2005).
[24] P. N. Juranić, J. Nordberg, and R. Wehlitz, Phys. Rev. A **74**, 042707 (2006).
[25] H. Aizawa, K. Wakiya, H. Suzuki, F. Koike, and F. Sasaki, J. Phys. B **18**, 289 (1985).
[26] A. Kupliauskiene, J. Phys. B **30**, 1865 (1997).
[27] C. Miron *et al.*, http://www.synchrotron-soleil.fr/portal/page/portal/Recherche/LignesLumiere/PLEIADES.
[28] F. Penent, J. Palaudoux, P. Lablanquie, L. Andric, R. Feifel, and J. H. D. Eland, Phys. Rev. Lett. **95**, 083002 (2005).
[29] P. Lablanquie, M. A. Khalal, L. Andric, J. Palaudoux, J-M. Bizau, F. Penent, D. Cubaynes, K. Jänkälä, Y. Hikosaka, K. Ito, K. Bučar, and M. Žitnik, J. Electron Spectrosc. Relat. Phenom. **220**, 125 (2017).
[30] K. Ito, F. Penent, Y. Hikosaka, E. Shigemasa, I. H. Suzuki, J. H. D. Eland, and P. Lablanquie, Rev. Sci. Instrum. **80**, 123101 (2009).
[31] F. A. Parpia, C. F. Fisher, and I. P. Grant, Comput. Phys. Commun. **94**, 249 (1996).
[32] S. Fritzsche, J. Electron Spectrosc. Relat. Phenom. **114**, 1155 (2001).
[33] S. Fritzsche, Phys. Scr. **2002**, 37 (2002).
[34] S. Fritzsche, Comput. Phys. Commun. **183**, 1525 (2012).
[35] A. Kramida, Yu. Ralchenko, and J. Reader, NIST ASD Team, *NIST Atomic Spectra Database* (version 5.8), available at https://physics.nist.gov/asd (National Institute of Standards and Technology, Gaithersburg, MD, 2020).
[36] See, for example, A. Kikas, A. Ausmees, M. Elango, J. N. Andersen, R. Nyholm, and I. Martinson, Europhys. Lett. **15**, 683 (1991).
[37] E. Kukk, G. Snell, J. D. Bozek, W.-T. Cheng, and N. Berrah, Phys. Rev. A **63**, 062702 (2001).
[38] S. Sheinerman, P. Lablanquie, F. Penent, Y. Hikosaka, T. Kaneyasu, E. Shigemasa, and K. Ito, J. Phys. B: At. Mol. Opt. Phys. **43**, 115001 (2010).
[39] J. Viefhaus, G. Snell, R. Hentges, M. Wiedenhöft, F. Heiser, O. Geßner, and U. Becker, Phys. Rev. Lett. **80**, 1618 (1998).

Correction: The name of the ninth author contained an error and has been fixed.